Ichise M, Liow JS, Lu JQ, Takano A, Model K, Toyama H, Suhara T, Suzuki K, Innis RB, Carson RE (2003) Linearized reference tissue parametric imaging methods: application to [11C]DASB positron emission tomography studies of the serotonin transporter in human brain. *J Cereb Blood Flow Metab* 23:1096–112

Ikoma Y, Ito H, Arakawa R, Okumura M, Seki C, Shidahara M, Takahashi H, Kimura Y, Kanno I, Suhara T (2008) Error analysis for PET measurement of dopamine D2 receptor occupancy by antipsychotics with [11C]raclopride and [11C]FLB 457. *Neuroimage* 42:1285–94

Inoue M, Suhara T, Sudo Y, Okubo Y, Yasuno F, Kishimoto T, Yoshikawa K, Tanada S (2001) Age-related reduction of extrastriatal dopamine D2 receptor measured by PET. *Life Sci* 69:1079–84

Jones JH, Anderson PS, Baldwin JJ, Clineschmidt BV, McClure DE, Lundell GF, Randall WC, Martin GE, Williams M, Hirshfield JM *et al* (1984) Synthesis of 4-substituted 2H-naphth[1,2-b]-1,4-oxazines, a new class of dopamine agonists. *J Med Chem* 27:1607–13

Kaasinen V, Nagren K, Hietala J, Farde L, Rinne JO (2001) Sex differences in extrastriatal dopamine d(2)-like receptors in the human brain. *Am J Psychiatry* 158:308–11

Kessler RM (2007) Aripiprazole: what is the role of dopamine D(2) receptor partial agonism? *Am J Psychiatry* 164:1310–2

Lammertsma AA, Hume SP (1996) Simplified reference tissue model for PET receptor studies. *Neuroimage* 4:153–8

Nelder JA, Mead R (1965) A simplex method for function minimization. *Comput J* 7:308–13

Neumeyer JL, Neustadt BR, Oh KH, Weinhardt KK, Boyce CB, Rosenberg FJ, Teiger DG (1973) Aporphines. 8. Total synthesis and pharmacological evaluation of (plus or minus)-apomorphine, (plus or minus)-apocodeine, (plus or minus)-N-n-propylnorapomorphine, and (plus or minus)-N-n-propylnorapocodeine. *J Med Chem* 16:1223–8

Ogden RT, Tarpey T (2006) Estimation in regression models with externally estimated parameters. *Biostatistics* 7:115–29

Otsuka T, Ito H, Halldin C, Takahashi H, Takano H, Arakawa R, Okumura M, Kodaka F, Miyoshi M, Sekine M, Seki C, Nakao R, Suzuki K, Finnema SJ, Hirayama Y, Suhara T, Farde L (2009) Quantitative PET analysis of the dopamine D2 receptor agonist radioligand 11C-(R)-2-CH3O-N-n-propylnorapomorphine in the human brain. *J Nucl Med* 50:703–10

Rosso L, Brock CS, Gallo JM, Saleem A, Price PM, Turkheimer FE, Aboagye EO (2009) A new model for prediction of drug distribution in tumor and normal tissues: pharmacokinetics of temozolomide in glioma patients. *Cancer Res* 69:120–7

Seneca N, Finnema SJ, Farde L, Gulyas B, Wikstrom HV, Halldin C, Innis RB (2006) Effect of amphetamine on dopamine D2 receptor binding in nonhuman primate brain: a comparison of the agonist radioligand [^{11}C]MNPA and antagonist [^{11}C]raclopride. *Synapse* 59:260–9

Seneca N, Skinbjerg M, Zoghbi SS, Liow JS, Gladding RL, Hong J, Kannan P, Tuan E, Sibley DR, Halldin C, Pike VW, Innis RB (2008) Kinetic brain analysis and whole-body imaging in monkey of [^{11}C]MNPA: a dopamine agonist radioligand. *Synapse* 62:700–9

Tokunaga M, Seneca N, Shin RM, Maeda J, Obayashi S, Okauchi T, Nagai Y, Zhang MR, Nakao R, Ito H, Innis RB, Halldin C, Suzuki K, Higuchi M, Suhara T (2009) Neuroimaging and physiological evidence for involvement of glutamatergic transmission in regulation of the striatal dopaminergic system. *J Neurosci* 29: 1887–96

Turkheimer F, Sokoloff L, Bertoldo A, Lucignani G, Reivich M, Jaggi JL, Schmidt K (1998) Estimation of component and parameter distributions in spectral analysis. *J Cereb Blood Flow Metab* 18:1211–22

Wu Y, Carson RE (2002) Noise reduction in the simplified reference tissue model for neuroreceptor functional imaging. *J Cereb Blood Flow Metab* 22:1440–52

Yokoi F, Grunder G, Biziere K, Stephane M, Dogan AS, Dannals RF, Ravert H, Suri A, Bramer S, Wong DF (2002) Dopamine D2 and D3 receptor occupancy in normal humans treated with the antipsychotic drug aripiprazole (OPC 14597): a study using positron emission tomography and [11C]raclopride. *Neuropsychopharmacology* 27:248–59

Eur J Nucl Med Mol Imaging (2009) 36:2014–2026
DOI 10.1007/s00259-009-1140-y

ORIGINAL ARTICLE

Non-invasive estimation of hepatic glucose uptake from [^{18}F] FDG PET images using tissue-derived input functions

N. Kudomi · M. J. Järvisalo · J. Kiss · R. Borra · A. Viljanen · T. Viljanen · T. Savunen · J. Knuuti · H. Iida · P. Nuutila · P. Iozzo

Received: 4 August 2008 / Accepted: 2 April 2009 / Published online: 13 June 2009

Abstract
Purpose The liver is perfused through the portal vein and hepatic artery. Quantification of hepatic glucose uptake (HGU) using PET requires the use of an input function for both the hepatic artery and portal vein. The former can be generally obtained invasively, but blood withdrawal from the portal vein is not practical in humans. The aim of this study was to develop and validate a new technique to obtain quantitative HGU by estimating the input function from PET images.
Methods Normal pigs (n=12) were studied with [^{18}F]FDG PET, in which arterial and portal blood time-activity curves (TAC) were determined invasively to serve as reference measurements. The present technique consisted of two characteristics, i.e. using a model input function and simultaneously fitting multiple liver tissue TACs from images by minimizing the residual sum of square between the tissue TACs and fitted curves. The input function was obtained from the parameters determined from the fitting. The HGU values were computed by the estimated and measured input functions and compared between the methods.
Results The estimated input functions were well reproduced. The HGU values, ranging from 0.005 to 0.02 ml/min per ml, were not significantly different between the two methods (r=0.95, p<0.001). A Bland-Altman plot demonstrated a small overestimation by the image-derived method with a bias of 0.00052 ml/min per g for HGU.
Conclusion The results presented demonstrate that the input function can be estimated directly from the PET image, supporting the fully non-invasive assessment of liver glucose metabolism in human studies.

Keywords [^{18}F]FDG PET · [^{18}F]FDG uptake kinetic modelling · Hepatic glucose uptake · Non-invasive · Input function

N. Kudomi (✉) · M. J. Järvisalo · R. Borra · A. Viljanen · T. Viljanen · J. Knuuti · P. Nuutila · P. Iozzo
Turku PET Centre, University of Turku,
P.O. Box 52, 20521 Turku, Finland
e-mail: nobuyuki.kudomi@tyks.fi

J. Kiss · T. Savunen
Department of Surgery, University of Turku,
Turku, Finland

H. Iida
Department of Investigative Radiology,
Advanced Medical Engineering Center,
National Cardiovascular Center-Research Institute,
5-7-1, Fujishirodai,
Suita, Osaka 565-8565, Japan

P. Nuutila
Department of Medicine, University of Turku,
Turku, Finland

P. Iozzo
Institute of Clinical Physiology, National Research Council,
56100 Pisa, Italy

Introduction

Abnormalities in hepatic glucose uptake (HGU) have been implicated in the pathogenesis of liver steatosis, hypertriglyceridaemia and diabetes [2, 6, 10]. Thus, HGU may become a prognostic indicator and useful marker during progression or treatment follow-up. Positron emission tomography (PET) in combination with [^{18}F]fluorodeoxyglucose ([^{18}F]FDG) is a potential tool to assess HGU, as shown by us and others in humans [4, 11] and animals [13, 18].

The liver is characterized by a dual blood supply, comprising the hepatic artery and the portal vein, draining

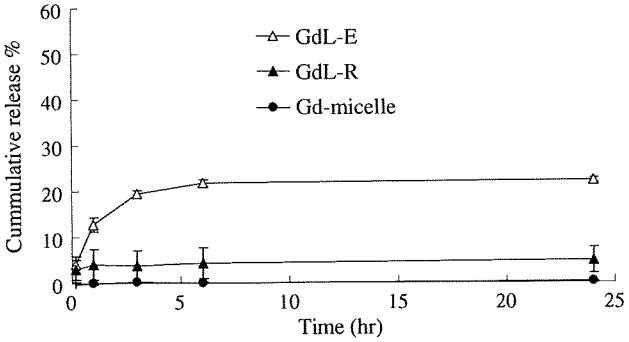

Fig. 2. Release profiles of Gd from Gd-micelle or Gd-DTPA from Gd-liposomes prepared by ethanol injection method (GdL-E) and reverse phase evaporation method (GdL-R) in PBS (pH 7.4) at 37°C. Data represent mean±S.D. (n=3).

Pharmacokinetics of the Gd-micelle and Gd-liposome

As shown in Fig. 3, at 10 min after the intravenous injection, 33.3% of the injected dose was found in blood for the Gd-micelle, and 40.0% and 50.3% for the Gd-liposome of GdL-E and GdL-R, respectively. At a dose of 33 μmol Gd/kg, the $T_{1/2}$ of the Gd-micelle was 10.2±3.9 h. Besides, the $T_{1/2}$ of GdL-E at a dose of 6.75 μmol Gd/kg and GdL-R at a dose of 2.65 μmol Gd/kg were 5.9±0.5 h and 6.0±1.0 h, respectively. In a previous study, we showed that Gd-DTPA was very rapidly cleared from the bloodstream with a minute's order half-life (19). Therefore, the detected Gd in blood is considered to be Gd-DTPA encapsulated in the liposome in a quantitative manner for measurements 6 h post intravenous injection. On the other hand, the main purpose of this study is the ABC phenomenon of a polymeric micelle MRI contrast agent, and PEGylated liposome is used as a positive control for the ABC phenomenon. Therefore, detection of liposome with Gd measurements is appropriate for the present purpose.

Effect of the First Dose on the Distribution of the Gd-micelle

The effects of the first dose on the distribution of the Gd-micelle injected a second time were evaluated. When the second dose of Gd-micelle was fixed at 33 μmol/kg, there was no significant difference of percent injected doses in plasma, kidney, and spleen between various first doses of the Gd-micelle from 0 to 100 μmol/kg (Fig. 4A). A dose of 100 μmol Gd/kg is the clinical dose of Gd-DTPA (17). Interestingly, the distribution of Gd-micelles in plasma, kidney, spleen and liver with the first injection of the empty liposome was similar to that with the first injection of saline. For the liver, the percent injected dose after a first dose of 33 μmol/kg and 100 μmol/kg was significantly higher than in the control saline group, possibly due to the incomplete elimination of the first dose of the Gd-micelle in liver at day 7 because of high doses of polymeric micelles (67.3 mg ~ 203.9 mg polymer/kg). The dose of 2 μmol Gd/kg of the Gd-micelle was the minimum at which Gd was detectable by means of ICP 6 h after injection. As shown in Fig. 4B, when the second dose of the Gd-micelle was decreased to 5 μmol/kg and 2 μmol/kg, the distribution was similar to that of 33 μmol/kg (Fig. 4A). Hence, the results showed that the tissue distribution of the Gd-micelle at the second dose of 33, 5, or 2 μmol/kg was not affected significantly except in liver by pre-administration of the Gd-micelle or the empty liposome. Although Gd in the first dose may interfere with the Gd accumulation in liver following the second dose injection, Gd-micelle as the first dose for micelle-forming properties are

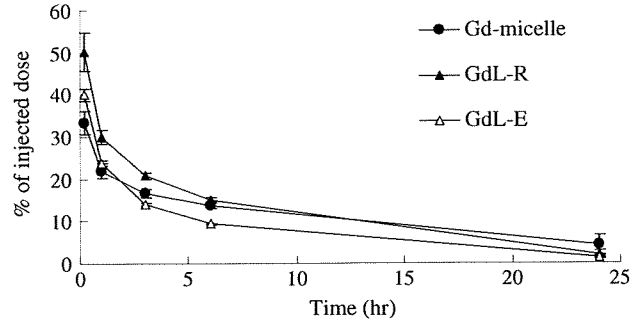

Fig. 3. Plasma elimination profiles of Gd following a single intravenous injection of Gd-micelle at a dose of 33 μmol Gd/kg and Gd-liposome including Gd-liposome prepared by ethanol injection method (GdL-E) at a dose of 6.75 μmol Gd/kg and Gd-liposome prepared by reverse phase evaporation method (GdL-R) at a dose of 2.65 μmol Gd/kg. Data represent mean±S.D. (n=3–4).

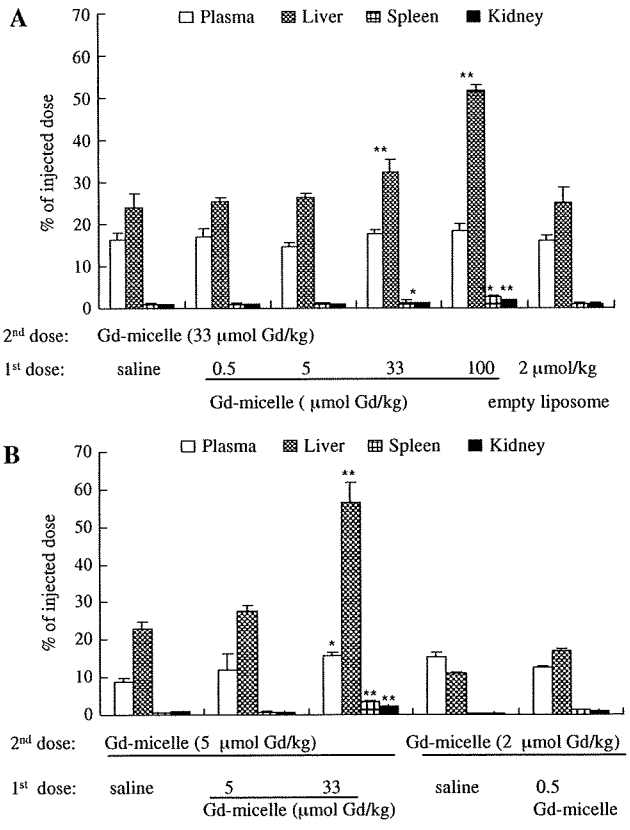

Fig. 4. Effect of the first dose on the tissue distribution of Gd-micelle. The second dose of Gd-micelle with 33 μmol/kg (**A**) or 5 μmol/kg or 2 μmol/kg (**B**) was intravenously injected at day 7 after the first injection of 0.5, 5, 33, 100 μmol/kg of Gd-micelle or the empty liposome at a dose of 2 μmol lipid/kg. Tissues including blood, liver, spleen, and kidney were taken out 6 h after the second injection of Gd-micelle. Data represent mean±S.D. (n=3, 6). P values apply to differences between the saline group and Gd-micelle or liposome treated group. *p<0.05, **p<0.01.

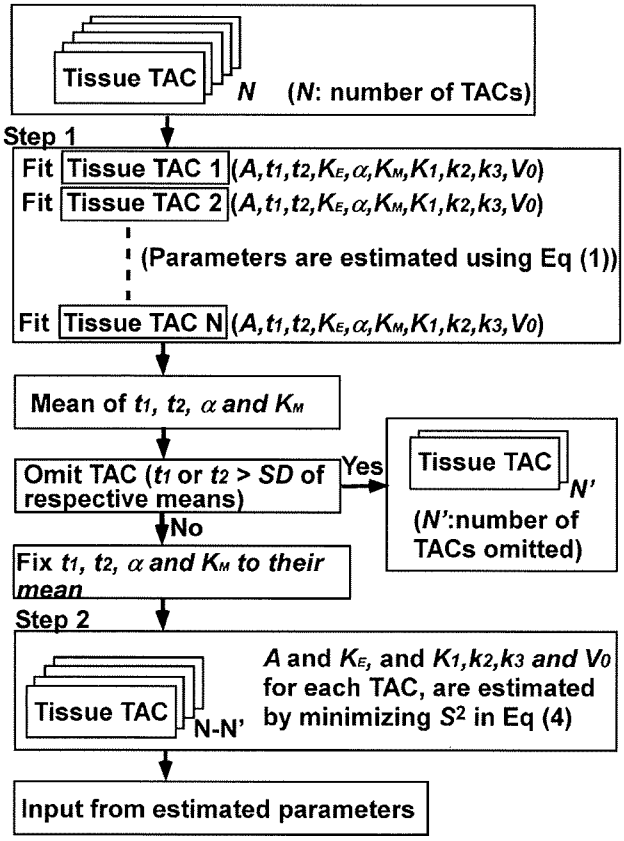

Fig. 1 A schematic diagram of the procedure to estimate the input functions using multiple tissue TACs. *Step 1*: the model function (Eq. 3) was individually fitted to N tissue TACs. Then, means and standard deviations of t_1, t_2, α and K_M were calculated, and the tissue TACs with values of t_1 or t_2>one standard deviation of respective means were excluded (indicated as N' TACs). In the *second step*, assuming that all parts of the liver share the same input functions, values of t_1, t_2, α and K_M were fixed to their means and the other two parameters (A and K_E) were estimated by minimizing Eq. 4 by the grid search method. Finally, the image-based input function was obtained by substituting the estimated parameters into Eq. 1

mization algorithm), and the set of ten parameters, A, t_1, t_2, K_E, α, K_M, K_1, k_2, k_3 and V_0, was obtained for each tissue TAC. Then, means and standard deviations of A, t_1, t_2, K_E, α and K_M were calculated, and the tissue TACs with values of t_1 or t_2>one standard deviation of respective means were excluded to avoid the potential influence of TACs outside the liver. In the second step, assuming that all parts of the liver share the same input function, values of t_1, t_2, α and K_M were fixed to their means and the other two parameters (A and K_E) in the model input function were estimated by minimizing the following equation:

$$S^2 = \sum_{i \in Tis} \sum_{k} \left(C_{Tis}^{i,k} - \left((1 - V_0^i) h^i(t) \otimes C_I(t) + V_0^i C_I(t) \right) \right)^2 \quad (4)$$

where $C_{\mathrm{Tis}}{}^{i,k}$ is the activity concentration for kth frame in ith tissue region of interest, t is the corresponding time of kth frame and $h^i(t)$ is defined as in Eq. 2 with rate constant values of K^i_1, k^i_2 and k^i_3, and blood volume of $V_0{}^i$, for ith tissue region, respectively. In this procedure, S^2 was minimized by the grid search method to avoid dependency on initial guess, where S^2 was calculated for 1,000 discrete values of both A and K_E between ranges of three standard deviations from respective mean values, omitting the negative value. In this procedure, for a given input function, i.e. once A and K_E are given, then K^i_1, k^i_2, k^i_3 and $V_0{}^i$ for ith TAC were computed by the Powell-Brent minimization algorithm, with acceptable ranges of 0–5 ml/min per g, 0–5 min^{-1}, 0–1 min^{-1} and 0–0.5 ml/ml, respectively, and then substituted into Eq. 4. Finally, the image-based input function was obtained by substituting the estimated parameters into Eq. 1.

Simulation study

The influence of noise versus number of TACs on the accuracy of the method was explored. As the noise on tissue TACs increased, the standard deviation of uptake ratio of tracer increased; as more regions were used, the standard deviation tended to decrease. However, if the number of TACs is larger, the noise on tissue is also large and vice versa. Our simulation was intended to reveal an optimal number of tissue TACs to be extracted from the whole region of the liver. First, to this purpose, we selected one mixed input function from one of the present experiments and used it as true input function in this simulation. One of the present experimental data sets was chosen and 100 tissue TACs were extracted as follows: a region of interest (ROI) was placed on the whole area of the liver in a summed image and subsequently divided into 100 subsets of TACs. The subsets were created as follows: first, the area under the curve (AUC) was computed for each pixel TAC. Second, TACs were ordered based on the AUC value and divided into 100 sets. Then, one TAC for each subset was obtained by averaging respective TACs. Each subset consisted of the same number of pixels. The rate constant values and blood volume (K_1, k_2, k_3 and V_0) were computed for each TAC using the corresponding input function by the non-linear Gauss-Newton method, assuming Eq. 3 and parameter values were obtained (means ± SDs were 1.4± 1.0 ml/min per g, 2.1±1.3 min^{-1}, 0.018±0.008 min^{-1} and 0.36±0.12 ml/ml for K_1, k_2, k_3 and V_0, respectively).

Based on the obtained set of rate constant values and blood volume, one set of 100 hepatic tissue TACs was generated from the true input function using Eq. 3. Then, tissue TACs with noise were generated as follows. Gaussian noise at peak was imposed on the set of 100 hepatic tissue TACs. Three levels of noise were introduced, corresponding to 10, 20 and 80% of counts at the level of the peak and 10, 20 and 80% of the square root of counts at the other points.

This procedure was repeated 100 times and 10,000 of noisy tissue TACs, embracing a total of 10,000 pixels, were obtained. Then, the TACs were ordered and averaged with the same procedure as in the experimental study (see below), i.e. the TACs were ordered based on the AUC and divided into N_{tis} (= 10, 15, 20, 50, 100 and 200) groups. The TACs were averaged for each group to obtain N_{tis} TACs. For each N_{tis} and each level of noise, input function was estimated, as described. Then, rate constant values were computed using estimated input function and tissue TACs. This procedure was repeated 100 times and the bias and deviation in values of rate constant values were calculated. Their bias and deviation were presented as a function of N_{tis}.

Experimental study

Study design

Details of the study design are given in previous articles [12, 13]. Briefly, after animal preparation, PET imaging was performed to measure liver glucose uptake during fasting (n=4), physiological (n=4) and supraphysiological (n=4) euglycaemic hyperinsulinaemia. [^{18}F]FDG was injected, and its concentration in the carotid artery and portal vein was frequently measured. Immediately after the animals were sacrificed, the liver was explanted to measure organ density. The protocol was reviewed and approved by the Ethics Committee for Animal Experiments of the University of Turku.

Animal preparation

Twelve anaesthetized, weight-matched pigs were studied during fasting (weight: 29.8±0.6 kg), physiological (1.0 mU · kg^{-1} · min^{-1}; weight: 30.0±0.5 kg) or supraphysiological euglycaemic hyperinsulinaemia (5.0 mU · kg^{-1} · min^{-1}; weight: 30.3±0.5 kg). Animals were deprived of food on the day before the study at 5 p.m. Anaesthesia was induced by injection of 1.0 g ketamine into the neck muscles before transportation of the pigs to the operating room. Throughout the experiment, animals were kept anaesthetized with ketamine and pancuronium (total of 1.5 g and 40 mg, respectively) and mechanically ventilated via tracheal intubation with oxygen and normal room air (regulated ventilation, 16 breaths/min). Catheters were placed in the femoral vein and carotid artery for the administration of glucose, insulin and [^{18}F]FDG and for sampling of arterial blood, respectively. Splanchnic vessels were accessed by subcostal incision; after dissection of the hepatogastric ligament, purse-string sutures were allocated to allow catheter insertion via a small incision in the portal vein. Doppler flow probes were placed around the portal vein and hepatic artery to monitor blood flow [12]. The surgical access was closed, and the distal catheter extremities were secured to the abdominal surface to avoid tip displacement. The animals were then transported to the PET Centre for tracer administration, liver imaging and blood sampling.

PET scanning

Scans were performed using an ECAT 931-08/12 scanner (CTI Inc., Knoxville, TN, USA). After acquisition of a transmission scan to correct for photon attenuation, [^{18}F]FDG (274±7 MBq) was rapidly injected, and an 180-min dynamic [^{18}F]FDG PET scan was started (31 frames, 8×15, 2×30, 2×120, 1×180, 6×300, 8×600 and 4×900 s). We sampled 2 ml of arterial and portal venous blood frequently (i.e. once every imaging time frame) for the determination of plasma [^{18}F]FDG radioactivity. The tube length was 260 mm. To keep tube patency, the line was flushed with a bolus of saline (5 ml), and a slow saline infusion was maintained. Vital signs, blood pressure and heart rate were monitored throughout the study.

Image processing

Dynamic sinogram data were corrected for dead time in each frame in addition to detector normalization. Random counts were also subtracted based on random counting obtained by the off-time coincidence method. Tomographic images were reconstructed from corrected sinogram data by the median root prior reconstruction algorithm (MRP) with 150 iterations and Bayesian coefficient of 0.3 [1]. Scatter correction was not available; however, the MRP can produce more accurate quantitative pixel values with high resolution and good noise reduction than filtered back projection (FBP) or maximum likelihood expectation maximization (MLEM) reconstruction algorithms, and reconstruction artefacts due to the FBP algorithm are reduced [1]. Attenuation correction was applied with transmission data. A reconstructed image had 128×128×15 matrix size with a pixel size of 2.4 mm×2.4 mm and 6.7 mm with 31 frames. Spatial resolution in this scanner is 6.7 mm (axial) and 6.5 mm (in-plane) full-width at half-maximum (FWHM). From this study, the first 60-min data, i.e. 21 frames, were used in the current analysis.

Data processing

Measured arterial ($C_a(t)$ Bq/ml) and portal ($C_p(t)$ Bq/ml) plasma TACs corrected for decay were mixed based on flow rates in hepatic artery (F_a ml/min) and portal vein (F_p ml/min), as determined by the ultrasonography technique, as follows: $(C_a(t)\cdot F_a + C_p(t)\cdot F_p)/(F_a + F_p)$. Then, the mixed

blood curve was corrected for delay by fitting to a whole liver tissue TAC based on a previous method [9], assuming a two-tissue compartment model.

An ROI was placed on the whole region of the liver in a summed image. The ROI for the whole region covered $(1.6\pm0.2)\times10^4$ pixels and was subsequently divided into 30 subsets of TACs. The subsets were created as follows: first, the AUC was computed for each pixel TAC. Second, TACs were ordered based on the AUC value and divided into 30 sets. Then, one TAC for each subset was obtained by averaging respective TACs. Each subset consisted of the same number of pixels. Representative TACs are shown in Fig. 2.

Then, the input function was estimated using TACs in each subset. In the first step, initial values and boundary conditions for the non-linear fitting for each parameter were 20,000 between 0.02 and 200,000,000 Bq/ml for A, 0.30 between 0.1 and 0.5 ml/min for K_E, 10 between −20 and 50 s for t_1, 60 between 50 and 80 s for t_2- t_1, 0.50 between 0.40 and 2.00 for α, 0.085 between 0.05 and 0.50 for K_M, 1.5 between 0.1 and 5 ml/min per g for K_1, 1.5 between 0.1 and 5 min^{-1} for k_2, 0.01 between 0.0001 and 1.0 min^{-1} for k_3 and 0.15 between 0 and 0.5 ml/ml for V_0, respectively. In the second step, the S^2 value in Eq. 4 was minimized, and the image-based input function was obtained. AUC for measured and image-based inputs were calculated for 0–60 min. Their % difference was calculated.

The rate values of K_1, k_2 and k_3 were computed by the non-linear fitting method (Gauss-Newton method) using the equation in combination with either the estimated input function obtained from the present method or blood withdrawal data. Then, hepatic fractional extraction values, $K_i=K_1k_3/(k_2+k_3)$, were calculated and compared between the two methods. Also, K_i values were computed by the Gjedde-Patlak analysis method [7, 21, 22, 26] and values were compared between methods.

Results

Simulation study

Figure 2 compares curves obtained from experimental data and simulated data assuming 10% noise level. They show similar shapes and distributions between the methods, demonstrating that the simulation reproduced experimental conditions.

The influence of noise and the number of tissue TACs, i.e. the size of bias and deviation on overall rate constant values, were minimal when the number of tissue TACs was 10–40 and the influence was independent of noise level (Fig. 3), although the optimal number of tissue TACs depended on the rate constants K_1, k_2, k_3 and K_i. The result suggested that the overall optimal number of tissue TACs to be applied to preserve accuracy is in the above range.

Among the six parameters A, t_1, t_2, K_E, α and K_M, the four parameters t_1, t_2 α and K_M were determined with the same accuracy, i.e. less than 1 s for t_1, less than 5 s for t_2, 5% for α and 7% for K_M, respectively, independent of the number of tissue TACs applied. The degree of deviation of the remaining two parameters depended on the number of parameters.

Experimental study

Reconstructed images are shown in Fig. 4.

The average of estimated delay time between the tissue curve and measured input was 15±13 s.

In the first step, one- or two-tissue TACs were excluded because the estimated t_1 value was smaller than the mean subtracted by one standard deviation. The t_1 value in these TACs were 8–16 s earlier than the mean, suggesting that these TACs were located in a region overlapping the vena cava. The estimated t_2- t_1 was 66±8 s, which was similar to the tracer administration duration.

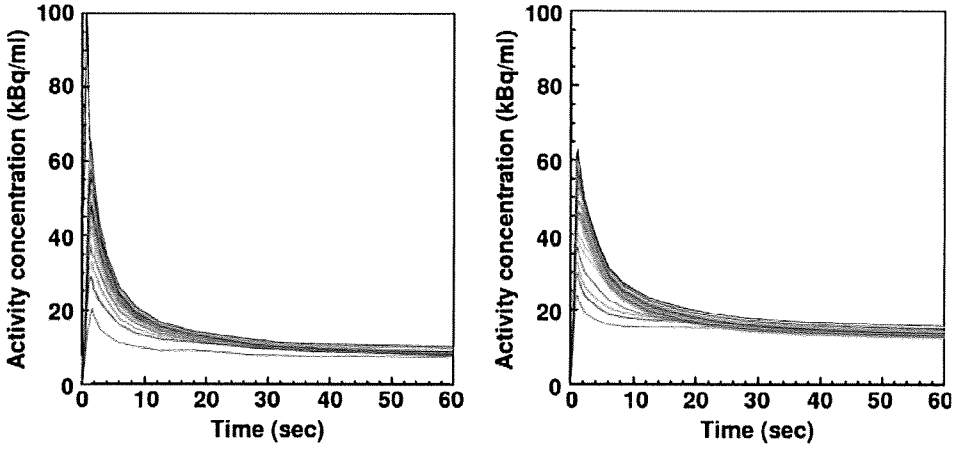

Fig. 2 Comparison of tissue curves obtained from experimental (*left*) and simulated data (*right*), showing similar shapes and distributions between the methods. The *black solid curve* with an extremely large peak in the early phase in the left panel is from a region covering the vena cava, distal to the injection site. The curve was excluded in the first step of the estimation procedure

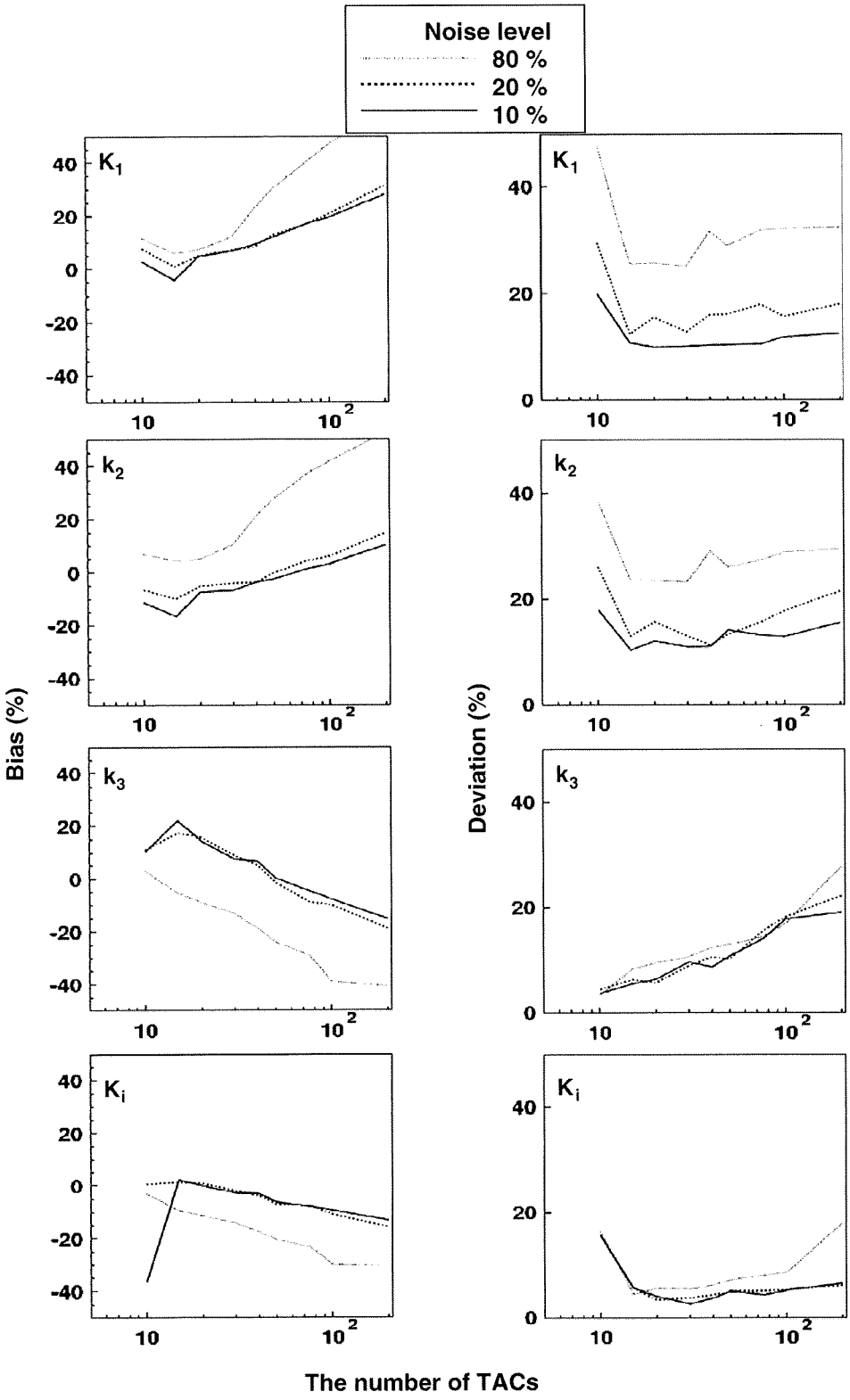

Fig. 3 Bias (*left*) and deviation (*right*) in the rate constant values of K_1, k_2, k_3 and K_i as a function of the number of time activity curves applied to the estimation of the input function

Figure 5 shows a representative fitted curve of the model input function (Eq. 3) directly fitted to the corresponding measured input function, suggesting that the model function was almost fully adequate to estimate the input.

Estimated, image-derived hepatic input functions are shown in Fig. 6. Those were almost identical to the measured curves. The mean ± SD of difference of AUC was −3.6±8.0%, ranging from −10.8 to 12.3%.

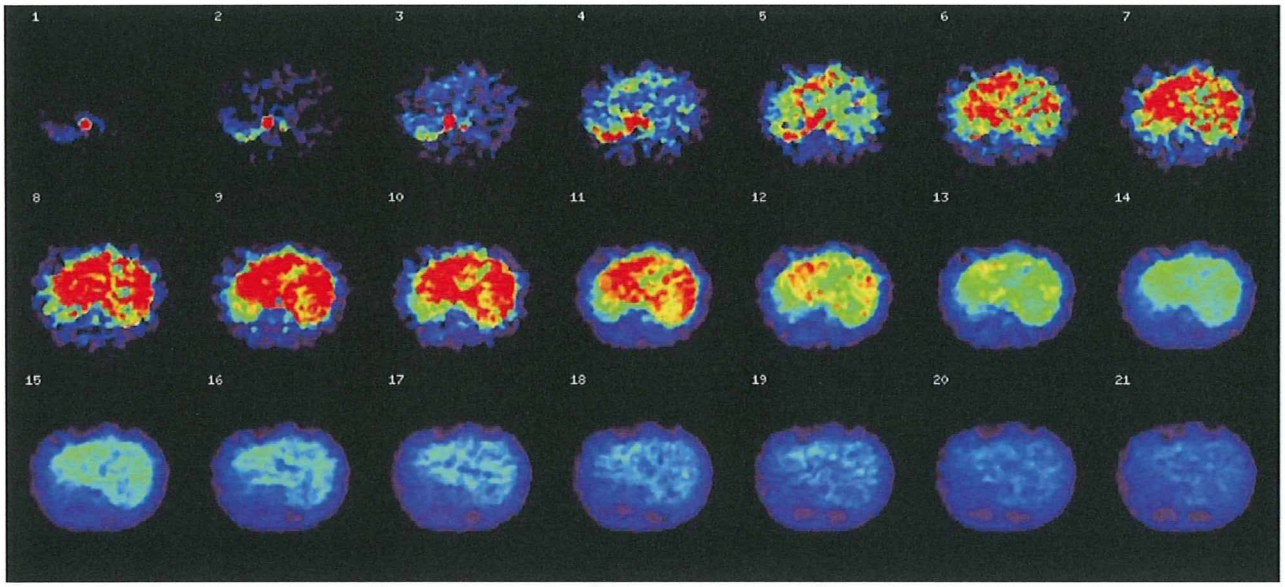

Fig. 4 Representative view of liver [^{18}F]FDG images obtained from one of the experimental studies. Each figure is represented in the same scale and slice at the *n*th frame, which is indicated in the *upper left corner* of each image

The relationships and Bland-Altman plots between values of hepatic K_1, k_2, k_3 and K_i, as estimated by using the image-derived versus the measured blood curves, are shown in Fig. 7. The plots demonstrate a small overestimation by the image-derived method, with a bias of 0.03 and 0.00052 ml/min per g for K_1 and K_i and of −0.043 and 0.00025 min^{-1} for k_2 and k_3, respectively. Respective regression lines were: $y=0.09+0.93x$ ($r=0.96$, $p<0.001$), $y=0.11+0.92x$ ($r=0.94$, $p<0.001$), $y=0.0010+1.05x$ ($r=0.96$, $p<0.001$) and $y=0.00052+0.91x$ ($r=0.95$, $p<0.001$) for K_1, k_2, k_3 and K_i, respectively. The paired t test showed no significant difference between the methods. Differences were 2.5±19.9%, 0.5±18.1%, 1.9±15.7% and 0.6±11.2% for K_1, k_2, k_3 and K_i values, respectively.

The regression line equation for K_i values by Gjedde-Patlak analysis was $y=-0.00078+1.11x$ ($r=0.89$, $p<0.001$) and the paired t test showed no significant difference between the methods. The difference between the methods was 6.2±18.1%.

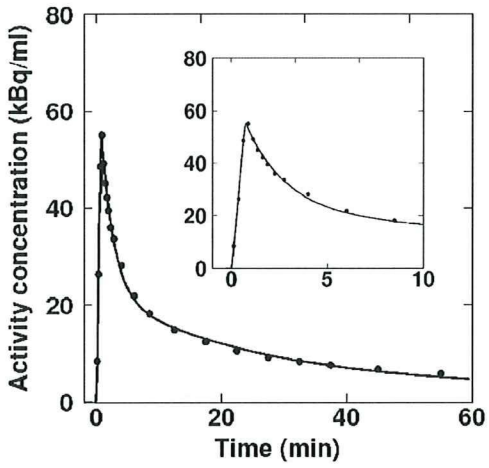

Fig. 5 TACs representing the mixed model input functions (Eq. 1), in comparison with the measured input function (*black circles*), generated by mixing the arterial and portal blood activity curves. The *inset* shows the input functions in the early phase

Discussion

In the current work, we validated a method to extract the mixed input function from liver [^{18}F]FDG PET images in experimental pig studies. The validity was shown in its coherence with measured input functions and in the tight correlation of hepatic glucose fractional extraction rate constant values between the present non-invasive method and the invasive blood sampling method. The results presented demonstrate that the input function can be estimated directly from PET images, supporting the fully non-invasive assessment of liver glucose metabolism in clinical applications. The perspective application attainable here is dual. On the one side, the comparison between measured arterial and estimated dual (arterial + portal) tracer levels provides indirect information on gut metabolism, and the gastrointestinal system is a metabolically active organ, manipulating ingested substrates and regulating their absorption. This apparatus is generally difficult to sample during imaging, due to its sparse location and thin walls, and the current approach could be used similar to a

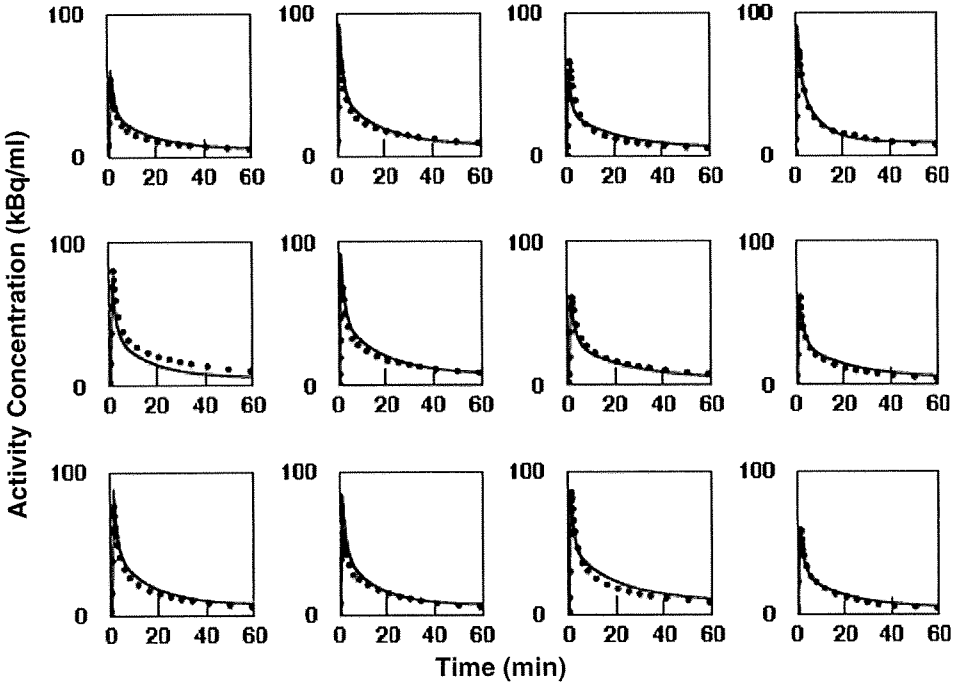

Fig. 6 Estimated input functions from PET images and their comparison with measured input (plot) functions

non-invasive arterial-venous balance through the organ. On the other side, the liver controls blood substrate levels, and its glucose uptake and phosphorylation appear to serve as signals for hepatic glucose release, also participating in the modulation of liver fatty acid and triglyceride metabolism. Thus, the assessment of HGU may be a target process in the pathogenesis and treatment of diabetes, dyslipidaemia and the metabolic syndrome.

The current approach estimated the hepatic input function from multiple tissue curves to calculate organ glucose uptake. A high degree of overlap and tight correlations were observed between the estimated input functions and those obtained by the blood sampling/counting during PET scans. Consequently, calculated rate constant values were consistent between the methods. The present approach was originally developed for hepatic perfusion studies with $H_2{}^{15}O$ PET [17], in which we documented optimal agreement between the estimated input functions and those obtained by the blood sampling/counting during PET scans, and between hepatic perfusion by PET and by ultrasonography. In our previous report, the arterial and portal inputs as well as the corresponding blood flow values were estimated separately because water could be assumed to be freely diffusible in the gut system and the variation in gut uptake rate constant was small enough to allow substitution of individual values with a fixed one. Thus, we could express the portal input uniquely from arterial input. In contrast, the extraction fraction of the current tracer ranged from 0.05 to 0.20 (*data not shown*) and the uptake rate constant value of [^{18}F]FDG in the gut system ranged from 0.20 to 0.80 min^{-1}, which cannot be replaced by an assumed common value. Furthermore, because the extraction fraction in the gut system is not 100%, and the shape of the arterial component flowing into the portal input and not being extracted could be assumed to be very similar to that of the arterial input, it is not feasible to distinguish the two contributions in mathematical formulations. Thus, the present method provides directly and solely a mixed input function.

As an alternative to the present procedure, a ROI-based input extraction from PET images has been used for the carotid artery in [^{11}C]flumazenil brain studies [24], the abdominal artery for kidney blood flow quantification with $H_2{}^{15}O$ [14], the aorta for cardiac [^{18}F]FDG metabolism [25] and for tumour blood flow using $H_2{}^{15}O$ [28]. In these approaches, ROIs are drawn in visible vessels and partial volume correction is needed; their application to HGU estimation is limited by the difficulty in identifying the portal vein in PET images. Closer to the current analysis, Di Bella et al. applied multiple tissue curves to estimate quantitative kinetic parameters in the brain [3], and reproduced the input function well for $H_2{}^{15}O$, showing the possibility to extract the input function from multiple tissue TACs, by assuming a single-tissue compartment model and a negligible blood volume component. The applicability of their method to the present [^{18}F]FDG liver study, which requires a two-tissue compartment model accounting for a large blood volume of 0.3 ml/ml [13], is unknown. Also, Sanabria-Bohórquez et al. [24] applied simultaneous fitting of multiple tissue TACs based on a

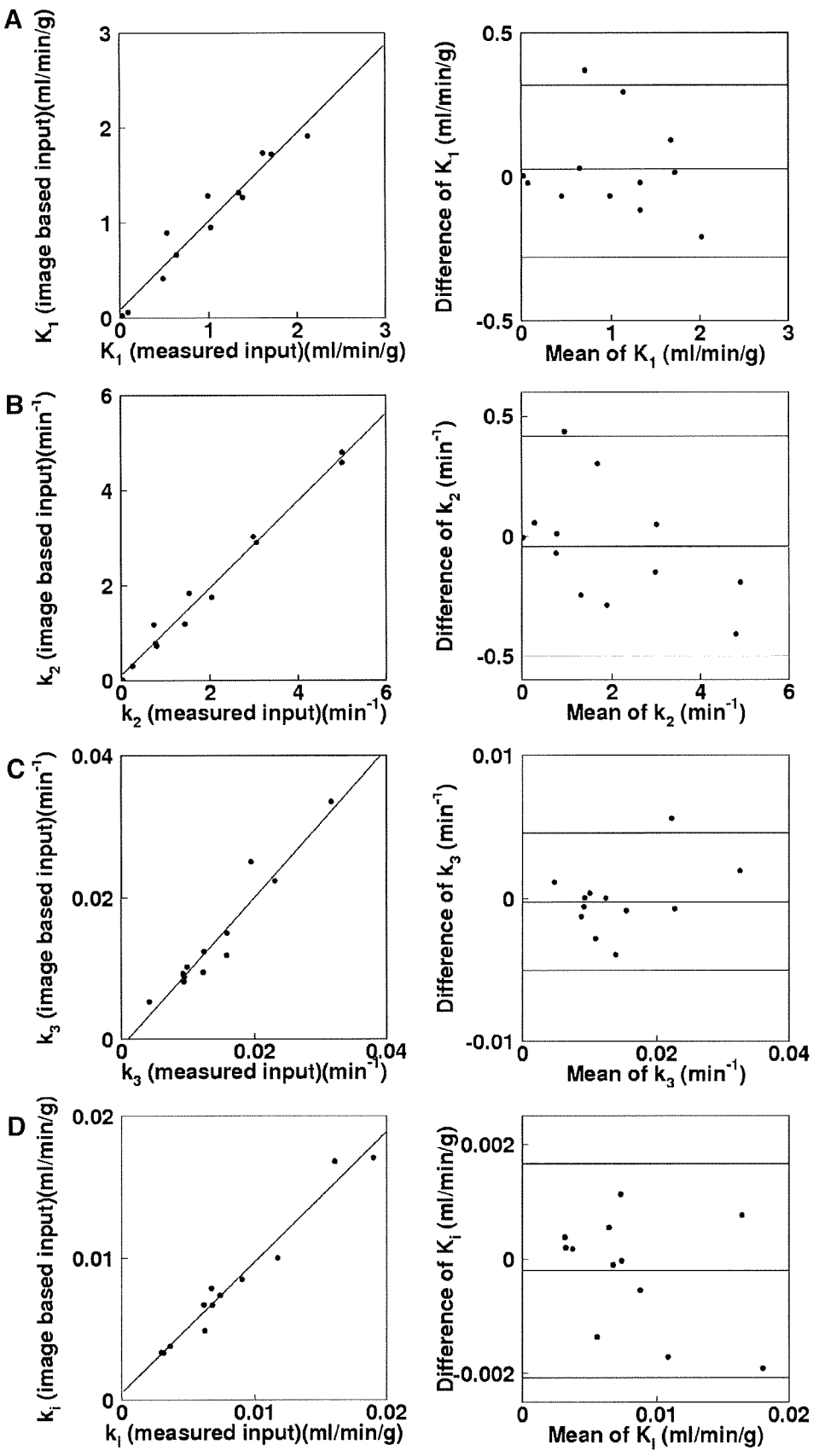

Fig. 7 Relationship (*left*) and Bland-Altman plot (*right*) between K_1 (**a**), k_2 (**b**), k_3 (**c**) and K_i (**d**) values, as estimated with measured and image-derived input functions. The *solid line* in *left figures* shows the regression line obtained, i.e. $y=0.09+0.93x$ ($r=0.96$, $p<0.001$), $y=0.11+0.92x$ ($r=0.94$, $p<0.001$), $y=0.0010+1.05x$ ($r=0.96$, $p<0.001$) and $y=0.00052+0.91x$ ($r=0.95$, $p<0.001$), for K_1, k_2, k_3 and K_i, respectively

mathematical description of a model input function similar to the present method and reproduced the input function well for [^{11}C]flumazenil. The method cannot be applied to HGU studies, because the formulae for the input function are partially based on the shape of image-derived curves from ROIs on visible carotid arteries. Otherwise, the shape of an arterial input function from multiple tissue TACs has been well reproduced in brain [^{18}F]FDG or [^{11}C]MPDX studies, by using an independent component analysis-based method (extraction of the plasma TAC using independent component analysis, EPICA) [19, 20], still requiring one arterial blood sample. The combination of the latter and the current techniques may provide a further simplification and deserves investigation, since it would entail neither a model function nor direct blood measurements.

One advantage of introducing a model function was to shape the curve of the input function by imposing constraints on the parameters range. We expect no relevant limitation in the extension of the assumptions concerning the shape to other species, and in a majority of hepatic conditions. A drawback in the use of a model function, however, is that the feasibility is unknown for a group in which the shape of input functions could be extremely different or cannot be expressed by the present model function. In this situation, the present method would require and may still be adapted to the use of group-specific parameter constraints or a modified model function. The present model function (Eq. 1) was created by assuming tracer bidirectional diffusion as well as metabolism in the whole body. The input functions obtained in the present study using this formula reproduced both the shape of measured inputs at the peak and the rate constant parameters well. In this study, the first 60-min data were used in the analysis, because most previous studies for quantification of HGU were performed using this scan duration (40 min: Iozzo et al. [11], 63 min: Choi et al. [4]). When the input functions were estimated using longer time data, the estimated input functions were almost superimposable until 90–120 min but they were higher thereafter; namely, only two input functions were overestimated by 5 and 10% for 90- and 120-min data, respectively, whereas a majority of input functions were overestimated, though still by 5–10%, for 180-min data. When estimation was limited to 40-min data, the height of the peak was 10–30% lower than that of measured input in three cases.

We considered the possibility to apply standardized input function methods, which assume that input function across subjects and conditions have an identical shape so that only a scaling factor is needed, which could be derived from the assessment of tracer concentrations in one or two blood samples. However, the input function shape varied depending on the injection procedure and the individual physiology of study animals. In fact, both the shapes and the scales were different (Fig. 6) among the weight-matched subjects used in the present study.

The present estimation procedure followed two steps, as designed to fit tissue curves individually and then simultaneously. The first step allowed careful exclusion of tissue TACs showing t_1 or t_2 values over one standard deviation from the mean, to eliminate the influence of radioactivity outside the liver region. In fact, in the experimental procedure, [^{18}F]FDG was injected into the femoral vein, draining into the vena cava, and the tracer was expected to show an early peak in the case of an anatomical overlap with the vena cava. The second step was introduced to facilitate the achievement of the convergence, by fixing the values of t_1, t_2, α and K_M to their calculated means (as shown in the simulation study, those parameters were less divergent than the remaining two parameters) to estimate the remaining two parameters. The shapes of input functions were reproduced and rate constant parameters of K_1, k_2, k_3 and K_i were consistent with those obtained by using measured inputs. Thus, the correlation among parameters, which may limit the identification of unique solutions due to local minima, did not seem to affect the estimation of HGU, though further study is required for optimization.

Although a close agreement was shown between estimated and measured input functions (Fig. 6), some modelled input functions showed over- and underestimations as compared to the measured ones, and the difference of the AUC was −3.6±8.0%, ranging from −10.8 to 12.3% between them. On the one side, this may be due to a model function-related error. On the other side, the difference may also be partly explained by inherent ultrasonography measurement error [from multiple measurements of flow data, the coefficient of variation was 13±5% for portal flow and 18±10% for hepatic arterial flow in this study (*data not shown*)], since ultrasonography defined the % hepatic input contributions from arterial and portal blood to construct the mixed input TAC from the measured data. However, we found tight correlations in rate constant values of K_1, k_2, k_3 and K_i (r=0.96, 0.94, 0.96 and 0.95, respectively, and p<0.001 for all), as computed by non-linear fitting assuming a two-tissue compartment model. There are two mathematical approaches used to quantify liver [^{18}F]FDG uptake and phosphorylation, i.e. graphical analysis [11, 18] and two-tissue compartment model [4, 11, 12, 18], the latter accounting for the potential dephosphorylation of [^{18}F]FDG-6-phosphate ([^{18}F]FDG-6P) occurring in hepatocytes. Both provide an estimation of a composite parameter (i.e. the fractional extraction of the tracer) intended as a unidirectional influx rate constant, which can be used to compute HGU once the lumped constant (LC) is known. Further studies are required to

compare quantitative accuracy obtained by different models by using our image-derived input approach.

The validation of the current approach, as obtained in this study, is especially valuable in the liver for multiple reasons. First, the inaccessibility of the portal vein prevents its direct blood sampling in humans. Arterial blood can be obtained, but blood counting requires corrections for dispersion [8] and delay [5, 9, 15, 16, 23, 27], and cross-calibration between PET scanner and radioactivity counter, which are all potential sources of errors. Second, HGU can be compromised both as a consequence and a cause of hepatic disease and may become a prognostic indicator and useful marker during progression or treatment follow-up.

In conclusion, our results demonstrate that the concentration of [^{18}F]FDG reaching the liver as input function can be estimated directly from tissue TACs obtained through dynamic [^{18}F]FDG PET imaging. The calculated HGU values using estimated and measured input functions were similar.

Acknowledgments The authors thank the technical staff of the Turku PET Centre for the efforts and skills dedicated to this project. The study was conducted within the "Centre of Excellence in Molecular Imaging in Cardiovascular and Metabolic Research" supported by the Academy of Finland, University of Turku, Turku University Hospital and Abo Academy. This work is part of the project Hepatic and Adipose Tissue and Functions in the Metabolic Syndrome (HEPADIP), which is supported by the European Commission as an Integrated Project under the 6th Framework Programme (contract LSHMCT-2005-018734). The study was further supported by grants from the Finnish Diabetes Foundation (P.I.), EFSD/Eli-Lilly (P.I.), Sigrid Juselius Foundation (N.K.), and Novo Nordisk Foundation (P.N.).

Appendix

A model function for hepatic input function for ^{18}FDG was created, by assuming a three-compartment model, in which the tracer is administered in a rectangular form and diffuses bidirectionally between arterial blood and whole-body peripheral tissue compartments. Part of the tracer is metabolized and accumulated in the third compartment. Differential equations for the model function ($C_I(t)$) can be expressed as;

$$\frac{dC_I(t)}{dt} = \frac{dF}{dt} - K_E C_I(t) + K_I C_{WB}(t) \tag{5}$$

$$\frac{dC_{WB}(t)}{dt} = K_E C_I(t) - K_I C_{WB}(t) - K_M C_{WB}(t) \tag{6}$$

$$\frac{dF}{dt} = A \quad (t_1 \le t \le t_2) \qquad 0 \quad (elsewhere) \tag{7}$$

where t_1 assumes the appearance time of administered tracer and t_2-t_1 represents the administration duration, A is scalar of input function. The equation F (Eq. 7) represents the bolus administration of tracer in the rectangular form with duration t_2-t_1. $C_{WB}(t)$ is the expected tracer concentration in whole-body peripheral tissues, K_E and K_I are bidirectional tracer diffusion rates between blood and peripheral tissue compartments, respectively, and K_M is the metabolic rate of the tracer in assumed whole body. Solving Eq. 6 for C_{WB} gives:

$$C_{WB}(t) = K_e e^{-(KI+KM)\cdot t} \int_0^t C_I(\tau) e^{(KI+KM)\cdot \tau} d\tau \tag{8}$$

The sum of Eq. 5 and a × Eq. 6 generates:

$$\frac{d(C_I(t) + aC_{WB}(t))}{dt} = \frac{dF}{dt} + (a-1)K_E(C_I + aC_{WB}) \tag{9}$$

where

$$a = (K_I/K_E - 1 + K_M/K_E)/2 + \sqrt{K_I/K_E + (K_I/K_E - 1 + K_M/K_E)^2}\Big/4 \tag{10}$$

Thus,

$$C_I(t) + aC_{WB}(t) = \frac{dF}{dt} \otimes \exp(-(1-a)K_E t) \tag{11}$$

where $\otimes$ indicates convolution integral. Substitution of C_{WB} from Eq. 8 into Eq. 11 after multiplying $e^{(KI+KM)\cdot t}$ gives:

$$e^{(KI+KM)\cdot t} C_I(t) + aK_E \int_0^t C_I(\tau) e^{(KI+KM)\cdot \tau} d\tau = e^{-(1-a)Ke\cdot t + (KI+KM)\cdot t} \int_0^t \frac{dF}{dt} e^{(1-a)Ke\cdot t} d\tau \tag{12}$$

Differentiation with respect to t after arrangement gives:

$$\left(\frac{K_I}{a} + K_E\right) C_I(t) + \frac{dC_I(t)}{dt} = \frac{K_I}{a} e^{-(1-a)Ke\cdot t} \int_0^t \frac{dF}{dt} e^{(1-a)Ke\cdot t} d\tau + \frac{dF}{dt} \tag{13}$$

Thus,

$$C_I(t) = \frac{K_I}{a} e^{-\beta \cdot t} \int_0^t e^{Ke \cdot (a-1) \cdot T + \beta \cdot T} \int_0^T \frac{dF}{dt} e^{Ke \cdot (1-a) \cdot \tau} d\tau dT + e^{-\beta \cdot t} \int_0^T \frac{dF}{dt} e^{Ke \cdot \beta \cdot \tau} d\tau \quad (14)$$

where $\beta=(K_I/a+K_E)$. Solving Eq. 14, we obtain:

$$\begin{aligned} C_1(t) &= 0. && (t < t_1) \\ &= A\left[\frac{1-\exp(\beta(t_1-t))}{\beta} + \frac{\alpha(1-\exp(\beta(t_1-t)))}{a(1-a)\beta} - \frac{\alpha(\exp(K_E(1-a)(t_1-t_2))-\exp(\beta(t_1-t)))}{a(1-a)\gamma}\right] && (t_1 < t < t_2) \\ &= \left[A\frac{\exp(\beta(t_2-t))-\exp(\beta(t_1-t))}{\beta} + \frac{\alpha(1-\exp(\beta(t_1-t_2)))}{a(1-a)\beta} + \frac{\alpha(\exp(K_E\beta(t_1-t_2))-\exp(\beta(t_1-t_2)))}{a(1-a)\gamma}\right. \\ &\quad \left. + \frac{\alpha(\exp(K_E(1-a)t_2)-\exp(K_E(1-a)t_1))(\exp(K_E(1-a)t)-\exp(\gamma t_2-\beta t)))}{a(1-a)\gamma}\right] && (t > t_2) \end{aligned} \quad (15)$$

where $\alpha= K_I/K_E$ and $\gamma=(K_I/a+aK_E)$.

References

1. Alenius S, Ruotsalainen U. Bayesian image reconstruction for emission tomography based on median root prior. Eur J Nucl Med 1997;24:258–65.
2. Basu A, Basu R, Shah P, Vella A, Johnson CM, Nair KS, et al. Effects of type 2 diabetes on the ability of insulin and glucose to regulate splanchnic and muscle glucose metabolism: evidence for a defect in hepatic glucokinase activity. Diabetes 2000;49: 272–83.
3. Di Bella EV, Clackdoyle R, Gullberg GT. (1999) Blind estimation of compartmental model parameters. Phys Med Biol 1999;44: 765–80.
4. Choi Y, Hawkins RA, Huang SC, Brunken RC, Hoh CK, Messa C, et al. Evaluation of the effect of glucose ingestion and kinetic model configurations of FDG in the normal liver. J Nucl Med 1994;35:818–23.
5. Eriksson L, Kanno I. Blood sampling devices and measurements. Med Prog Technol 1991;17:249–57.
6. Ferre T, Riu E, Franckhauser S, Agudo J, Bosch F. Long-term overexpression of glucokinase in the liver of transgenic mice leads to insulin resistance. Diabetologia 2003;46:1662–8.
7. Gjedde A. Calculation of cerebral glucose phosphorylation from brain uptake of glucose analogs in vivo: a re-examination. Brain Res 1982;257:237–74.
8. Iida H, Kanno I, Miura S, Murakami M, Takahashi K, Uemura K. Error analysis of a quantitative cerebral blood flow measurement using H2(15)O autoradiography and positron emission tomography, with respect to the dispersion of the input function. J Cereb Blood Flow Metab 1986;6:536–45.
9. Iida H, Higano S, Tomura N, Shishido F, Kanno I, Miura S, et al. Evaluation of regional differences of tracer appearance time in cerebral tissues using [15O] water and dynamic positron emission tomography. J Cereb Blood Flow Metab 1988;8:285–8.
10. Iozzo P, Hallsten K, Oikonen V, Virtanen KA, Kemppainen J, Solin O, et al. Insulin-mediated hepatic glucose uptake is impaired in type 2 diabetes: evidence for a relationship with glycemic control. J Clin Endocrinol Metab 2003;88:2055–60.
11. Iozzo P, Geisler F, Oikonen V, Maki M, Takala T, Solin O, et al. Insulin stimulates liver glucose uptake in humans: an 18F-FDG PET Study. J Nucl Med 2003;44:682–9.
12. Iozzo P, Gastaldelli A, Järvisalo MJ, Kiss J, Borra R, Buzzigoli E, et al. 18F-FDG assessment of glucose disposal and production rates during fasting and insulin stimulation: a validation study. J Nucl Med 2006;47:1016–22.
13. Iozzo P, Jarvisalo MJ, Kiss J, Borra R, Naum GA, Viljanen A, et al. Quantification of liver glucose metabolism by positron emission tomography: validation study in pigs. Gastroenterology 2007;132:531–42.
14. Juillard L, Janier M, Fouque D, Lionnet M, Le Bars D, Cinotti L, et al. Renal blood flow measurement by positron emission tomography using 15O-labeled water. Kidney Int 2000;57: 2511–8.
15. Kanno I, Iida H, Miura S, Murakami M, Takahashi K, Sasaki H, et al. A system for cerebral blood flow measurement using an H215O autoradiographic method and positron emission tomography. J Cereb Blood Flow Metab 1987;7:143–53.
16. Kudomi N, Choi E, Watabe H, Kim KM, Shidahara M, Ogawa M, et al. Development of a GSO detector assembly for a continuous blood sampling system. IEEE Trans Nucl Sci 2003;50:70–73.
17. Kudomi N, Slimani L, Järvisalo MJ, Kiss J, Lautamäki R, Naum GA, et al. Non-invasive estimation of hepatic blood perfusion from H2 15O PET images using tissue-derived arterial and portal input functions. Eur J Nucl Med Mol Imaging 2008;35: 1899–911.
18. Munk OL, Bass L, Roelsgaard K, Bender D, Hansen SB, Keiding S. Liver kinetics of glucose analogs measured in pigs by PET: importance of dual-input blood sampling. J Nucl Med 2001;42: 795–801.
19. Naganawa M, Kimura Y, Nariai T, Ishii K, Oda K, Manabe Y, et al. Omission of serial arterial blood sampling in neuroreceptor imaging with independent component analysis. Neuroimage 2005;26:885–90.
20. Naganawa M, Kimura Y, Ishii K, Oda K, Ishiwata K, Matani A. Extraction of a plasma time-activity curve from dynamic brain PET images based on independent component analysis. IEEE Trans Biomed Eng 2005;52:201–10.
21. Patlak CS, Blasberg RG, Fenstermacher JD. Graphical evaluation of blood-to-brain transfer constants from multiple-time uptake data. J Cereb Blood Flow Metab 1983;3:1–7.

22. Patlak CS, Blasberg RG. Graphical evaluation of blood-to-brain transfer constants from multiple-time uptake data. Generalizations. J Cereb Blood Flow Metab 1985;5:584–90.
23. Ruotsalainen U, Raitakari M, Nuutila P, Oikonen V, Sipilä H, Teräs M, et al. Quantitative blood flow measurement of skeletal muscle using oxygen-15-water and PET. J Nucl Med 1997;38: 314–9.
24. Sanabria-Bohórquez SM, Maes A, Dupont P, Bormans G, de Groot T, Coimbra A, et al. Image-derived input function for [11C]flumazenil kinetic analysis in human brain. Mol Imaging Biol 2003;5:72–8.
25. van der Weerdt A, Klein LJ, Boellaard R, Visser CA, Visser FC, Lammertsma AA. Image-derived input functions for determination of MRGlu in cardiac (18)F-FDG PET scans. J Nucl Med 2001;42:1622–9.
26. Varga J, Szabo Z. Modified regression model for the Logan plot. J Cereb Blood Flow Metab 2002;22:240–4.
27. Votaw JR, Shulman SD. Performance evaluation of the Pico-Count flow-through detector for use in cerebral blood flow PET studies. J Nucl Med 1998;39:509–15.
28. Watabe H, Channing MA, Riddell C, Jousse F, Libutti SK, Carrasquillo JA, et al. Noninvasive estimation of the aorta input function for measurement of tumor blood flow with. IEEE Trans Med Imaging 2001;20:164–74.

Eur J Nucl Med Mol Imaging (2009) 36:683–691
DOI 10.1007/s00259-008-0994-8

ORIGINAL ARTICLE

Parametric renal blood flow imaging using [^{15}O]H_2O and PET

Nobuyuki Kudomi · Niina Koivuviita · Kaisa E. Liukko · Vesa J. Oikonen · Tuula Tolvanen · Hidehiro Iida · Risto Tertti · Kaj Metsärinne · Patricia Iozzo · Pirjo Nuutila

Received: 14 May 2008 / Accepted: 17 October 2008 / Published online: 3 December 2008

Abstract
Purpose The quantitative assessment of renal blood flow (RBF) may help to understand the physiological basis of kidney function and allow an evaluation of pathophysiological events leading to vascular damage, such as renal arterial stenosis and chronic allograft nephropathy. The RBF may be quantified using PET with $H_2{}^{15}O$, although RBF studies that have been performed without theoretical evaluation have assumed the partition coefficient of water (p, ml/g) to be uniform over the whole region of renal tissue, and/or radioactivity from the vascular space (V_A, ml/ml) to be negligible. The aim of this study was to develop a method for calculating parametric images of RBF (K_1, k_2) as well as V_A without fixing the partition coefficient by the basis function method (BFM).
Methods The feasibility was tested in healthy subjects. A simulation study was performed to evaluate error sensitivities for possible error sources.
Results The experimental study showed that the quantitative accuracy of the present method was consistent with nonlinear least-squares fitting, i.e. $K_{1,BFM}=0.93K_{1,NLF}-0.11$ ml/min/g ($r=0.80$, $p<0.001$), $k_{2,BFM}=0.96k_{2,NLF}-0.13$ ml/min/g ($r=0.77$, $p<0.001$), and $V_{A,BFM}=0.92V_{A,NLF}-0.00$ ml/ml ($r=0.97$, $p<0.001$). Values of the Akaike information criterion from this fitting were the smallest for all subjects except two. The quality of parametric images obtained was acceptable.
Conclusion The simulation study suggested that delay and dispersion time constants should be estimated within an accuracy of 2 s. V_A and p cannot be neglected or fixed, and reliable measurement of even relative RBF values requires that V_A is fitted. This study showed the feasibility of measurement of RBF using PET with $H_2{}^{15}O$.

Keywords Positron emission tomography · Renal blood flow · Compartment model · Parametric image

N. Kudomi (✉) · K. E. Liukko · V. J. Oikonen · T. Tolvanen · P. Iozzo · P. Nuutila
Turku PET Centre, University of Turku,
P.O. Box 52, FIN-20521 Turku, Finland
e-mail: nobuyuki.kudomi@tyks.fi

N. Koivuviita · R. Tertti · K. Metsärinne · P. Nuutila
Department of Medicine, University of Turku,
Turku, Finland

H. Iida
Department of Investigative Radiology,
Advanced Medical-Engineering Center,
National Cardiovascular Center-Research Institute,
5-7-1, Fujishirodai,
Suita, Osaka 565-8565, Japan

P. Iozzo
Institute of Clinical Physiology, National Research Council,
56100 Pisa, Italy

Introduction

The quantitative assessment of renal blood flow (RBF) may help to understand the pathophysiological basis of kidney function and to evaluate pathophysiological events leading to vascular damage, such as renal arterial stenosis and chronic allograft nephropathy. The quantitative estimation of RBF by the use of $H_2{}^{15}O$ and dynamic PET has been developed and demonstrated by Nitzsche et al. [1]. The kinetic model of $H_2{}^{15}O$ is based on the assumptions that all activity is extracted by the parenchyma, extraction is very rapid, and tubular transport has not started or is insignificant at a level that does not influence the calculation of RBF [1–5]. With these assumptions, RBF has been estimated based on regions of interest (ROI) by the $H_2{}^{15}O$

dynamic PET approach [1, 3, 4]. Also, calculations to produce parametric images of RBF has been reported [5]. However, the quantitative computation of RBF has so far assumed that the blood/tissue partition coefficient of water (p, ml/g) is uniform for the whole region of renal tissue [3, 4], and/or that the contribution of radioactivity from the vascular space is negligible [5–7]. The influence on quantitative accuracy of these assumptions is unknown.

In previous studies RBF has been computed from the uptake rate (K_1, ml/min/g) [1–7]. Some studies also simultaneously computed the partition coefficient (p) [6, 7], and the apparent p values obtained ranged between 0.52 and 0.78 ml/g. From the published values of water content for tissue (76%) and blood (81%) [8], the p value can be physiologically determined as: p_{phys}=0.94 ml/g [9]. The much smaller apparent p value might be due to the tissue mixture (or a partial volume effect) [10, 11] because of the composite structure of the kidney. The effects of the tissue mixture affect mostly K_1 and not clearance rate (k_2 min^{-1}). Therefore the clearance rate of $H_2{}^{15}O$ (k_2 min^{-1}) multiplied by p_{phys} could be used for the calculation of blood flow rather than K_1 (ml/min/g) [11] when the effect of the tissue mixture is not negligible, although it is unknown how the glomerular filtration rate (GFR) additionally contribute to k_2. Thus, the influence of GFR on k_2 should be evaluated and allowed for in the computation of RBF.

The aim of this study was to develop a method to simultaneously calculate parametric images of K_1 and k_2 as well as the arterial blood volume (V_A, ml/ml). The feasibility in terms of quantitative accuracy and image quality of calculated images was experimentally tested in healthy subjects. GFR was measured in each subject to investigate how much it contributes to the clearance rate (k_2, min^{-1}). A simulation study was also performed to evaluate error sensitivities for possible error sources.

Materials and methods

Theory

The present formula was characterized by simultaneously estimating multiple parameters of uptake rate constant (K_1, ml/min/g) and clearance rate constant (k_2 ml/g) as well as activity concentration in the arterial vascular space (V_A, ml/ml). The kinetic model for $H_2{}^{15}O$ was based on a single-tissue compartment model as follows:

$$Ci(t) = (1 - V_A) \cdot K_1 \cdot A_w(t) \otimes e^{-k2 \cdot t} + V_A \cdot A_w(t) \qquad (1)$$

where $Ci(t)$ (Bq/ml) is radioactivity concentration in a voxel of PET image, $A_w(t)$ (Bq/ml) is the arterial input function, and $\otimes$ indicates the convolution integral.

In the present computation, we applied a basis function method (BFM) as introduced by Koeppe et al. [12] to compute the cerebral blood flow parametric image as well as the clearance rate constant simultaneously. Gunn et al. [13] applied this method to parametric imaging of both binding potential and the delivery of ligand relative to the reference region. The computation method has also been applied to myocardial blood flow studies to compute the uptake, clearance rates and blood volume [14, 15]. The BFM procedure for the present RBF computation is illustrated in Fig. 1. The BFM method enables parametric images to be computed by using linear least squares together with a discrete range of basis functions as the parameter value for k_2 incorporating the nonlinearity and covering the expected physiological range. The corresponding basis functions formed are:

$$F(k_2, t) = A_w(t) \otimes e^{-k2 \cdot t} \qquad (2)$$

For a physiologically reasonable range of k_2, i.e. $0 < k_2 < 15.0$ ml/min/g, 1,500 discrete values for k_2 were found to

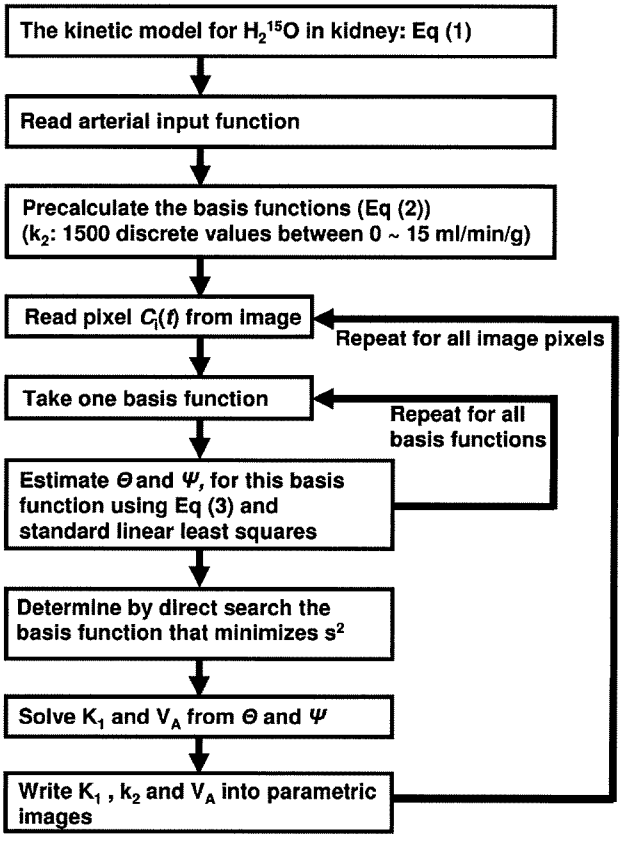

Fig. 1 Schematic diagram of the computation procedure by the BFM

be sufficient. Then Eq. 1 can be transformed for each basis function into a linear equation:

$$\begin{aligned} Ci(t) &= \Theta \cdot F(k_2, t) + \Psi \cdot A_w(t) \\ \Theta &= (1 - V_A) \cdot K_1 \\ \Psi &= V_A \end{aligned} \quad (3)$$

Hence for fixed values of k_2, the remaining two parameters Θ and Ψ can be estimated using the given basis function by standard linear least squares, and are represented as Θ_{k2} and Ψ_{k2}. The value k_2 for which the residual sum of squares

$$s(k_2)^2 = \sum_t (Ci(t) - \Theta_{k2} \cdot F(k_2, t) - \Psi_{k2} \cdot A_w(t))^2 \quad (4)$$

is minimized is determined by a direct search, and associated parameter values for this solution (K_1, k_2, V_A) are obtained.

Subjects

Six healthy human subjects (the demographics are shown in Table 1) were studied under basal conditions and stimulation (after enalapril infusion) conditions. All subjects were nonsmokers and none of them was taking any medication. All subjects gave written informed consent. The study was approved by the Ethics Committee of the Hospital District of South-Western Finland, and was conducted in accordance with the Declaration of Helsinki as revised in 1966.

Table 1 Baseline characteristics of the six subjects studied

Characteristic	Mean±SD
Age (years)	58±5
Plasma creatinine (μmol/l)	85±10
Estimated GFR (ml/min)[a]	78±4
Weight (kg)	82.8±4.5
Body mass index (kg/m^2)	26.6±2.2
Blood pressure (mmHg)	
Systolic	136±11
Diastolic	82±4
Heart rate (min^{-1})	57±5
Fasting plasma total cholesterol (mmol/l)	5.3±1.0
Fasting plasma high density cholesterol (mmol/l)	1.5±0.4
Fasting plasma triglycerides (mmol/l)	1.2±0.4
Fasting plasma low density cholesterol (mmol/l)	3.2±0.8
Blood haemoglobin (g/l)	144±12
Fasting plasma glucose (mmol/l)	5.4±0.4

[a] Estimated according to the Modification of Diet in Renal Disease study equation.

PET experiments

PET was carried out in 2-D mode using a GE Advance scanner (GE Medical Systems, Milwaukee, WI). After a 300-s transmission scan, two scans were undertaken with injection of $H_2{}^{15}O$ (1.0 to 1.5 GBq) into the cephalic vein of the right forearm. The first scan was under resting conditions and the other was under stimulated conditions, namely 20 min after infusion of 0.5 mg enalapril. The scan protocol consisted of 20 frames over a total of 240 s (15×4 s, and 5×10 s). During PET scanning, blood was withdrawn continuously through a catheter inserted into the left radial artery using a peristaltic pump (Scanditronix, Uppsala, Sweden). Radioactivity concentrations in the blood were measured with a BGO coincidence monitor system. The detectors had been cross-calibrated to the PET scanner via an ion chamber [16]. GFR was also measured in each subject [17]. To obtain the PET equivalent flow ratio for GFR, a kidney weight of 300 g and a cortex ratio of 70% were assumed [8].

Data processing

Dynamic sinogram data were corrected for dead time in each frame in addition to detector normalization. Tomographic images were reconstructed from corrected sinogram data by the OSEM method using a Hann filter with a cut-off frequency of 4.6 mm. Attenuation correction was applied with the transmission data. A reconstructed image consisted 128×128×35 matrix size with a pixel size of 4.3×4.3 mm and 4.2 mm with 20 frames. Measured arterial blood time–activity curves (TAC) were calibrated to the PET scanner and corrected for the dispersion (τ=5 and 2.5 s for intrinsic and extrinsic, respectively) [18] and delay [19]. The corrected blood TAC was used as the input function.

A set of K_1, k_2 and V_A images was generated according to the BFM formula described above, using a set of dynamic reconstructed images and input function. Computations were programmed in C environment (gcc 3.2) on a Sun workstation (Solaris 10 Sun Fire 280R) with 4 GB of memory and two Sparcv9, 900-MHz CPUs.

Data analysis

A template ROI obtained by summing whole frames of a reconstructed dynamic image was drawn on an image of the whole region of each kidney (average ROI size for the all subjects was 153±43 cm^3). Also, a ROI was drawn on a region of high tracer accumulation on the summed image as an assumed cortical region. Functional values of K_1, k_2 and V_A were extracted from both ROIs, i.e. for the whole region and the cortical region, respectively. Data re shown individually or as means±SD. Student's paired t test was

used for comparisons between the physiological states and p values <0.05 were considered significant.

The ROI for the whole region was divided plane-by-plane into subregions of ten pixels each. The subregions were created by extracting pixels first from the horizontal direction and then from the vertical direction inside the whole ROI in each slice. Each subregion consisted of a single area with the same number of pixels. Functional values of K_1, k_2 and V_A were extracted from each subregion. Tissue TACs were also obtained for each subregion from corresponding dynamic images. The three parameters K_1, k_2 and V_A were estimated using the Eq. 1 and the input function fitted to the tissue TACs by the nonlinear least-squares fitting method (NLF, Gauss-Newton method). Functional values of K_1, k_2 and V_A from corresponding subregions were then compared between the methods. Regression analysis was performed.

The model relevancy introducing p and/or V_A into the computation was tested using the Akaike Information Criterion (AIC) [20]. The most appropriate model provides the smallest AIC. The tissue TACs from the subregions were fitted and AICs were computed for models with the three parameters K_1, k_2 and V_A, fixing p ($=K_1/k_2$) at 0.35 ml/g (mean value obtained in the present subjects), fixing V_A at 0 ml/ml, and fixing V_A at 0.15 ml/ml (mean value obtained in the present subjects).

Error analysis in the simulation

Error propagation from errors in the input function for the present BFM formula was analysed for two factors: delay and dispersion in arterial TAC. It is known that the measured arterial TAC is delayed and more dispersed relative to the true input TAC in the kidney because of the time for transit of blood through the peripheral artery and the catheter tube before reaching the detector [18, 19]. Calculations of RBF so far have employed a fixed partition coefficient (p, $=K_1/k_2$, ml/g) and/or assumed the blood volume (V_A, ml/ml) as negligible throughout the whole renal region and do not estimate it regionally. BFM formulae with a fixed value of p (BFM-pfix) and blood volume V_A (BFM-vfix) in addition to the present BFM formula, and the error in these formulae, were analysed.

A typical arterial input function obtained from the present PET study was used in the present simulation as the true input function. Applying this input function to the water kinetic model in Eq. 1, a tissue TAC was created assuming values for normal kidney tissue (K_1=2.0 ml/min/g, V_A=0.14 ml/g [5], and p=0.4 ml/g, corresponding to the estimated means in cortical region in all subjects in this study).

Time in the input function was shifted from −4 to 4 s to simulate the error sensitivity due to the error in the time delay, where a positive error represents an over-correction of the time delay. The input function was convoluted or deconvoluted with a simple exponential [18] by shifting the time constant from −4 to 4 s to simulate the error sensitivity due to error in dispersion correction, where a negative error represents under-correction, as described previously [18, 21]. Values of K_1 and k_2 were calculated using simulated input functions and the tissue TACs based on the BFM formula. Errors in these calculated K_1 and k_2 values are presented as percentage differences from the assumed values. Then, the value of p was varied from 0.3 to 0.5 ml/g and the tissue TAC was generated as above to simulate the error from the value of p in BFM-pfix formula. Also, the V_A value was varied from 0.0 to 0.4 ml/ml and the tissue TAC was generated to simulating the error from V_A in BFM-vfix formula. Then, K_1 and k_2 were calculated using the true input function and the created tissue TACs, assuming p=0.4 ml/g and V_A=0.0 ml/ml in the BFM-pfix and BFM-vfix formulae, respectively. Error in K_1 and k_2 values due to fixing p is presented as the percentage difference in K_1 and k_2 as a function of p. Error in K_1 and k_2 values due to neglecting V_A is presented as the percentage difference in K_1 and k_2 as a function of V_A. Also, K_1 and k_2 were computed with V_A fixed at 0.14 ml/ml in the BFM-vfix formula from the set of the tissue TACs, in which K_1 and p were fixed at 2.0 ml/min/g and 0.4 ml/g, respectively, and V_A was varied. The percentage difference in K_1 and k_2 between the two conditions, i.e. the initial (K_1=2.0 ml/min/g and V_A=0.14 ml/ml) and changed conditions (presented as ΔK_1 and Δk_2, respectively) is presented as a function of the percentage difference in the assumed V_A from 0.14 ml/ml (ΔV) to investigate the extents to which the change in K_1 and k_2 were estimated when K_1 and k_2 were computed in the BFM-vfix formula.

Results

Experiments

The relationships of the regional ROI values of K_1, k_2 and V_A between NLF and BFM are shown in Fig. 2. The regression lines obtained were $K_{1,BFM}=0.93K_{1,NLF}-0.11$ ml/min/g (r=0.80, p<0.001), $k_{2,BFM}=0.96k_{2,NLF}-0.13$ ml/min/g (r=0.77, p<0.001), and $V_{A,BFM}=0.92V_{A,NLF}-0.00$ ml/ml (r=0.97, p<0.001), where the subscripts show the methods used for calculating the parametric values; the slopes were not significantly different from unity.

The fitted curve by the present model estimating K_1, k_2 and V_A fitted better than the other two models fixing p ($=K_1/k_2$) or V_A. An example of fitted curves is shown in Fig. 3. Also, the AIC values from three parameter fitting were the smallest for all subjects except two values for two

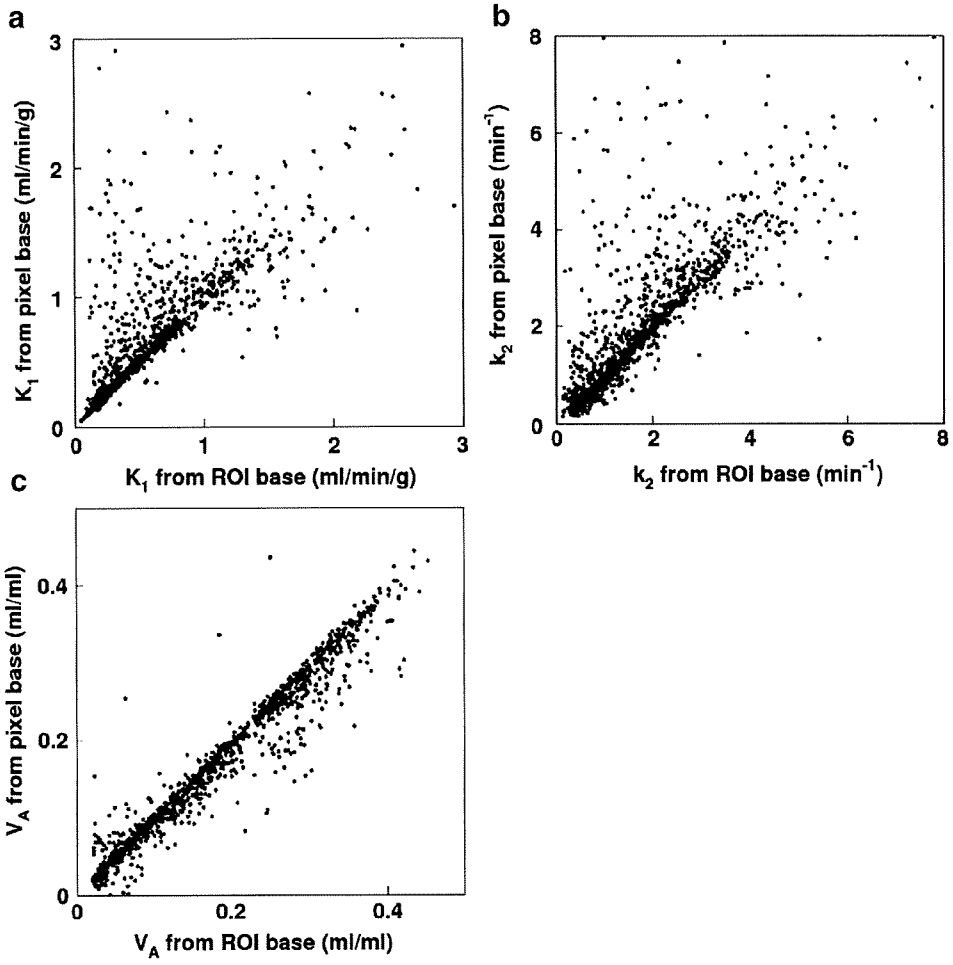

Fig. 2 Relationships of (**a**) K_1, (**b**) k_2 and (**c**) V_A between the ROI-based NLF method and pixel-based BFM. The regression lines were $K_{1,BFM}=0.93K_{1,NLF}-0.11$ ml/min/g ($r=0.80$, $p<0.001$), $k_{2,BFM}=0.96k_{2,NLF}-0.13$ ml/min/g ($r=0.77$, $p<0.001$), and $V_{A,BFM}=0.92V_{A,NLF}-0.00$ ml/ml ($r=0.97$, $p<0.001$)

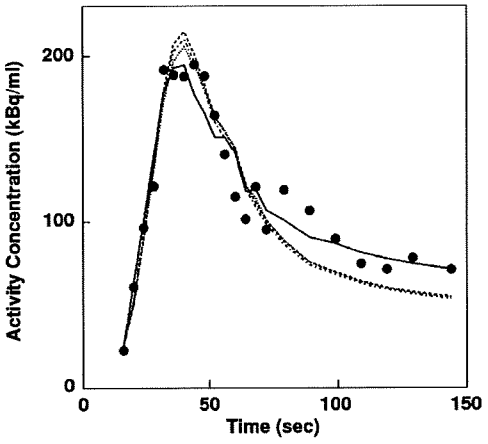

Fig. 3 Curves fitted to the measured tissue TAC from the different computation methods. Three parameters: K_1, k_2 and V_A were computed. p-fixed: K_1 and V_A were computed with p ($=K_1/k_2$) fixed at 0.35 ml/g. V_A-fixed: K_1 and k_2 were computed with V_A fixed at 0.15 ml/g. V_A-ignored: K_1 and k_2 were computed without taking into account V_A

parameter fitting fixing V_A in patient 2 and fixing p in patient 3, although some AIC values were similar (Table 2). These results show that the present method with three parameter fitting is feasible for computing RBF.

Values of K_1, $k_2 \cdot p_{phys}$ and V_A were obtained for the whole renal region and cortical region (Table 3). The K_1

Table 2 AIC values for the models

Subject	Three parameters[a]	p-fixed[b]	V_A-fixed (0.15)[c]	V_A-ignored[d]
1	484±20	519±28	499±15	494±15
2	474±9	486±14	474±9	477±8
3	525±12	523±8.3	527±10	527±7
4	483±14	497±21	501±12	506±13
5	497±18	502±19	508±32	499±13
6	496±11	507±14	500±9	497±9

[a] K_1 and k_2, V_A computed.
[b] K_1 and V_A computed with k_2 fixing such that $p=K_1/k_2=0.35$ ml/g.
[c] K_1 and k_2 computed with V_A fixed at 0.15 ml/g.
[d] K_1 and k_2 computed without taking into account V_A.

Table 3 Values of K_1, $k_2 \cdot p_{phys}$ and V_A (n=6) in the whole renal region and the cortical region calculated by the present method for the baseline conditions and the stimulated conditions

	K_1 (ml/min/g)	$k_2 \cdot p_{phys}$ (ml/min/g)	V_A (ml/ml)	GFR (ml/min/g)
Whole region				
Baseline	1.09±0.33	3.11±1.48	0.15±0.09	0.35±2[a]
Enalapril-stimulated	1.03±0.44	2.55±1.29	0.16±0.14	
Cortical region				
Baseline	1.57±0.60*	3.64±2.15*	0.18±0.12*	
Enalapril-stimulated	1.42±0.39*	3.55±1.64*	0.25±0.14*	

No significant difference was found between the baseline and stimulated conditions.
*Difference was significant between the whole and cortical regions.
[a] A kidney weight of 300 g and a cortex ratio of 70% were assumed.

values were smaller than $k_2 \cdot p_{phys}$ values and the ratio between them ranged from 0.35 to 0.45, suggesting that K_1 values underestimated RBF due to the partial volume effect. Both K_1 and $k_2 \cdot p_{phys}$ were not significantly different between the resting and stimulated conditions for the whole renal region and the cortical region, respectively, although the value of V_A was higher under the stimulated conditions than under the basal conditions. The GFR obtained was 78±4 ml/min, corresponding to a clearance rate of 0.37±0.02 ml/min/g and to 9.6% of the k_2 obtained for the cortical region under the normal conditions.

Representative K_1 and $k_2 \cdot p_{phys}$ images generated by the present method are shown in Fig. 4. The quality of the image is acceptable. The K_1 and $k_2 \cdot p_{phys}$ values ranged from 1.5 to 2.0 ml/min/g and 3.0 to 5.0 around cortical region, respectively, and some parts showed higher values than these. The average time required to compute the parametric images was 2 min 23 s.

Error analysis

The sizes of the errors introduced in both K_1 and k_2 were less than 20% for estimation of delay and the dispersion time constant up to 2 s (Fig. 5). The error sensitivity in K_1 and k_2 was 40% when the partition coefficient was 0.35 (Fig. 6). The magnitude of the error was markedly enhanced when the blood volume was ignored (Fig. 7a), and if the arterial blood volume increased by 25%, K_1 and k_2 were overestimated by 20% (Fig. 7a).

Discussion

We have presented an approach to generating quantitative K_1, k_2 and V_A images using $H_2{}^{15}O$ and PET applying the BFM computation method. The validity of this approach in healthy human subjects under resting and stimulated conditions is described. The rate constant values of K_1 and $k_2 \cdot p_{phys}$ obtained from the parametric images were consistent against NFL and the quality of the K_1 and $k_2 \cdot p_{phys}$ images obtained was acceptable. The smaller K_1 against $k_2 \cdot p_{phys}$ values suggested that the K_1 values underestimated the absolute RBF value due to the partial volume effect. The simulation showed that the delay time and dispersion time constant should be estimated within an accuracy of 2 s, and V_A and p cannot be ignored/fixed to

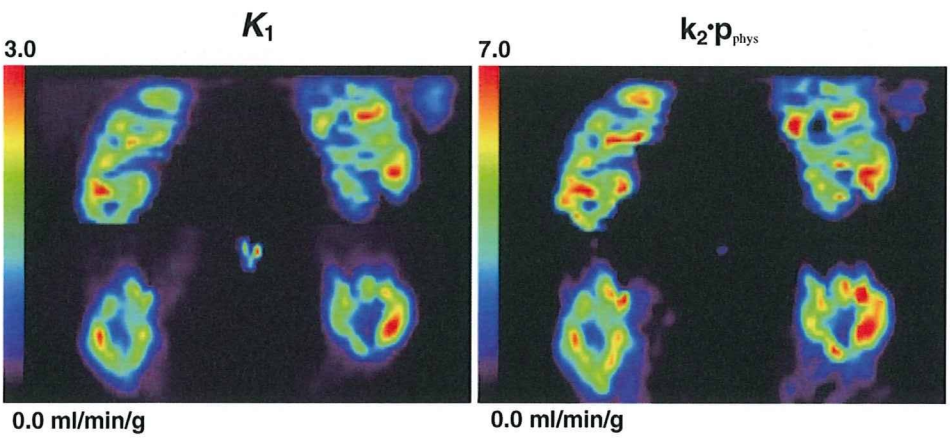

Fig. 4 Representative parametric images of K_1 (*left*) and $k_2 \cdot p_{phys}$ (*right*) for a subject under baseline conditions. Coronal (*upper*) and transverse (*lower*) views are shown